BNL-228943-2025-JAAM

Magnetically Tunable Polariton Cavities in van der Waals Heterostructures

R. Mayer, L. Wehmeier

To be published in "Nano Letters"

September 2025

Photon Sciences

Brookhaven National Laboratory

U.S. Department of Energy

USDOE Office of Science (SC), Basic Energy Sciences (BES). Scientific User Facilities (SUF)

Magnetically tunable polariton cavities in van der Waals heterostructures

Rafael A. Mayer[1,2,3,*], Xinzhong Chen[1,4], Ran Jing[1,5], Makoto Tsuneto[1], Boyi Zhou[1,6], Zijian Zhou[1], Wenjun Zheng[1], Rui Pu[1], Suheng Xu[4], Tom Liu[1], Helen Yao[7,8], Lukas Wehmeier[9], Yinan Dong[4], Dihao Sun[4], Leo He[4], Alisson R. Cadore[10,12], Tony Heinz[8,11], Jonathan A. Fan[7], Cory R. Dean[4], D. N. Basov[4], Xu Du[1], Raul O. Freitas[2,*], Mengkun Liu[1,9,*]

[1]Department of Physics and Astronomy, Stony Brook University, Stony Brook, NY, 11794, USA. [2]Brazilian Synchrotron Light Laboratory (LNLS), Brazilian Center for Research in Energy and Materials (CNPEM), 13083-970, Campinas, Sao Paulo, Brazil. [3]Instituto de Física Gleb Wataghin, Universidade Estadual de Campinas (UNICAMP), 13083-859, Campinas, Sao Paulo, Brazil. [4]Department of Physics, Columbia University, New York, NY, 10027, USA. [5]Condensed Matter Physics and Materials Science Division, Brookhaven National Laboratory, Upton, NY, 11973, USA. [6]Center for Integrated Science and Engineering, Columbia University, New York, NY, 10027, USA. [7]Department of Materials Science and Engineering, Stanford University, Stanford, CA, 94305, USA. [8]SLAC National Accelerator Laboratory, Menlo Park, CA, 94025, USA. [9]National Synchrotron Light Source II, Brookhaven National Laboratory, Upton, NY, 11973, USA. [10]Brazilian Nanotechnology National Laboratory (LNNano), Brazilian Center for Research in Energy and Materials (CNPEM), 13083-970, Campinas, Sao Paulo, Brazil. [11]Department of Applied Physics, Stanford University, Stanford, CA, 94305, USA. [12]Programa de Pós-Graduação em Física, Instituto de Física, Universidade Federal de Mato Grosso, 78060-900, Cuiabá, Mato Grosso, Brazil

*Corresponding authors.

✉email: rafael.mayer@lnls.br, raul.freitas@lnls.br and mengkun.liu@stonybrook.edu

Nanophotonic cavities are the foundation for a broad spectrum of applications, including quantum sensing, on-chip communication, and cavity quantum electrodynamics. In van der Waals (vdW) materials, these cavities can harness polaritons—quasiparticles emerging from photon interactions with excitons, plasmons, or phonons that are confined in microscopic sample flakes. Hybrid phonon-plasmon cavities leverage the long lifetimes of phonons and good tunability of plasmons, but their reconfigurability remains fundamentally limited. Here, we introduce a magnetic-field tuning mechanism for polaritonic cavities in a van der Waals heterostructure. Specifically, we demonstrate that the primary Landau transition in magnetized charge-neutral graphene can be harvested for controlling polaritonic cavity modes in a graphene-based phononic heterostructure. Additionally, we predict a magnetic field-induced topological transition in the polariton isofrequency contour, causing a non-trivial cavity mode profile re-distribution. Our study underscores the versatility of Landau-based nanophotonic cavities, offering new paradigms for the design and manipulation of light-matter interactions at the nanoscale.

Keywords: Nanophotonics, polaritons, Magneto-optics, Graphene, van der Waals, Landau transitions

Optical cavities have been fundamental to enabling many breakthroughs in science, from lasers to Rabi oscillations in atoms[1]. Traditionally, they consist of partially reflective structures that trap photons of specific frequencies. Due to self-interference, these cavities can concentrate electromagnetic fields to extreme values, facilitating the investigation of hybrid states of light and matter named polaritons. In two-dimensional (2D) crystals, in-plane propagating polaritons can naturally form from the hybridization of photons with fundamental resonances of matter, such as phonons, plasmons, excitons, etc[2]. Due to their extreme field confinement, polaritons in 2D systems have enabled many potential applications at the nanoscale, such as negative refraction[3–5], light canalization[6–8], and hyperlensing[9]. Their quasi-2D character, and therefore small mode volumes, have also enabled an enhanced sensitivity in near-field experiments, which can be critical for probing weak oscillators such as vibrational modes of a single molecule[10]. Modern photonics has combined the classical microcavity approach with 2D polaritonics to miniaturize optical cavities down to subdiffractional volumes. By imposing additional spatial restrictions to the 2D systems (e.g. a 3D confinement), one can form a polaritonic cavity of enormous field enhacement[11]. Thus, the research on tunable polaritonic cavities is essential for advancing the control of chemical reactions[12], nonlinear optics[13,14], and quantum electrodynamics[15].

Polaritonic cavities made of polar materials such as hexagonal boron nitride (hBN) and alpha molybdenum trioxide (α-MoO_3) host low loss and extremely confined hyperbolic phonon polaritons (HPhPs), which can result in high quality factors[16,17]. Particularly, the biaxial nature of α-MoO_3 provides an additional spatial control of polariton propagation[18,19], allowing for the tuning of the cavity mode distribution. However, phonons are intrinsically difficult to tune. Previous efforts have utilized surface plasmon polaritons (SPPs) in graphene as an electrically gateable system for HPhPs in other vdW materials[20–23]. Although vastly explored, the tuning range of phonon-SPP devices is fundamentally limited by the dielectric breakdown of the insulating layer. For instance, in graphene/hBN/SiO_2 (300nm)/Si devices, the polariton wavelength at 1395 cm^{-1} (within hBN's Reststrahlen band) can be increased to 13% of its original value when 100 V gate voltage is applied[22], nearing the breakdown of oxide layer.

Here, we explore the strong coupling between HPhPs in α-MoO_3 cavities and the ***primary*** Landau level transition in magnetized charge-neutral graphene. We demonstrate that these systems support quasi-particles, termed Landau Phonon Polaritons (LPPs)[24], which exhibit extreme wavelength tunability. As an example, application of a 6 T field at 880 cm^{-1} produces a 41% shift in the polariton wavelength. This value is prohibitive through electric gating in our heterostructures, as it would require a 0.59 eV increase in Fermi energy for graphene in zero field. To confine the LPPs, we use a truncated biaxial heterostructure composed of an α-MoO_3 ribbon and hBN-encapsulated graphene. We image real-space interference profiles of polaritons configured by the cavity resonances utilizing a home-built magneto scattering-type scanning near-field microscope (hereafter referred to as m-SNOM), which operates at magnetic fields up to 7 T. The resulting LPPs manifest as Fabry-Perot resonances, as the HPhPs are confined by the walls of the α-MoO_3 ribbon. We demonstrate that both the cavity resonances and their quality factor are tunable with the magnetic field, opening possibilities for nanocavities of higher dynamic range. Moreover, we predict that the spatial distribution of the cavity modes is easily adjustable due to a magnetic-induced topological transition that occurs in the LPP isofrequency contour (IFC).

Figure 1a illustrates the m-SNOM setup used to image the cavity modes in our device. The m-SNOM includes a metal-coated atomic force microscopy (AFM) tip, which is illuminated by an infrared (IR) beam. The tip-scattered field is detected and demodulated to yield the near-field response[25]. This process allows us to simultaneously measure topographic and electromagnetic response of samples with a spatial resolution of ~10 nm. Additionally, the confined fields near the tip apex enables coupling to polariton modes at finite momentum. [26,27]. The AFM and illuminating/collecting optics are mounted inside a closed-cycle cryo-chamber equipped with a split-coil superconducting magnet (see Methods for details).

The sample consists of a 50 nm-thick α-MoO_3 on top of a hBN/graphene/hBN stack, assembled through the pick-up transfer technique (see Methods for details). An additional thin layer of hBN covers the entire device to enhance the surface mechanical stability of α-MoO_3 at low temperatures[28]. The vdW heterostructure rests on a SiO_2/Si substrate and includes electric contacts that enable tuning of the graphene Fermi energy (Figure S7 from Supporting Information shows the optical image of the device). When a magnetic field is applied perpendicularly to the plane of graphene, the charges undergo cyclotron motion and quantize the graphene's Dirac bands into Landau Levels (LL), as illustrated in Figure 1b. The energy of the LL in graphene is given by $E_n = \mathrm{sgn}(n)\sqrt{2|n|}\left(\frac{\hbar v_F}{l_B}\right)$, where $n = 0, \pm 1, \pm 2, \ldots$ is the LL index, v_F is graphene Fermi velocity and l_B is the magnetic length, defined as $l_B = \sqrt{\hbar/\mathrm{e}|B|}$. Due to the lifting of the spin and valley degeneracy at low temperature and high fields, the zeroth LL would show finer structures. Compared to the photon energy ($E_{ph} \sim 100\ meV$) that we use in this experiment, the energy scales of these finer structures are small enough to be neglected[29,30]. When photons with an energy $E_{ph} = \left|E_i - E_j\right|$, where i and j are the initial and final levels index, and $|i| - |j| = \pm 1$ (for "allowed" transitions), interact with graphene, they create a pair of electron-hole, thus generating Dirac magneto-excitons (DiME)[31]. This work utilizes the first LL transition ($i = \pm 1$ and $j = 0$), which is expected to exhibit the strongest oscillator strength at IR frequencies[32] and has not yet been explored in the context of hybridized polaritonics. While electrostatic gating operates in the weak coupling regime with a broadband Drude response, the LPPs fall into the strong coupling regime, providing greater tunability due to the significant conductivity at resonance with the Landau level transition.

Figure 1c displays the real part of graphene longitudinal optical conductivity σ_{xx} as a function of the photon frequency and the magnetic field. The conductivity of graphene reaches a peak when $E_{ph} \approx \left|E_{\pm 1} - 0\right| = v_F\sqrt{2e\hbar|B|}$. As we demonstrate later in the text, we can exploit this feature to fine-tune polaritonic resonances with the magnetic field. To generate cavity LPPs, we couple the DiME modes of graphene to HPhPs in α-MoO_3. The HPhPs occur when at least two components of the real part of the dielectric tensor have opposite signs. As shown in Figure 1d, this occurs in the mid-IR range at three different bands for the α-MoO_3. Notably, around 830 cm^{-1} to 920 cm^{-1}, the HPhPs exhibit in-plane hyperbolicity and, consequently, propagate with concave wavefronts at preferable directions[33]. By coupling graphene's DiME with α-MoO_3's HPhP, we can engineer the topology of LPP IFC to be magnetically tunable[34–36].

Near-field images of MoO_3/Graphene hybrid polaritons show strong magnetic dependences. Figures 1e-f show near-field images at 880 cm^{-1} under different magnetic fields: B = 0 T (295 K), B=4 T (150 K), and at B = 7 T (150 K). To highlight cavity resonances, we also present the averaged signal along the [100] direction of the α-MoO_3 crystal, referenced here as the x-axis. The [001] and [010] directions are referenced throughout the text as y-, and z-axes, respectively. At 0 T we observe four vertical stripes. As the magnetic field increases to 4T, the hybridization between HPhPs and DiMEs reduces the number of near-field maxima to three. Even though E_{ph} is far from E_1 at 4 T, as illustrated in Figure 1c, the variation in graphene's conductivity is sufficient to drive a modification in the LPP dispersion due the large bandwidth of E_1. At 7 T, the cavity modes cannot be clearly discerned, as the polaritonic mode is gapped out by DiME.

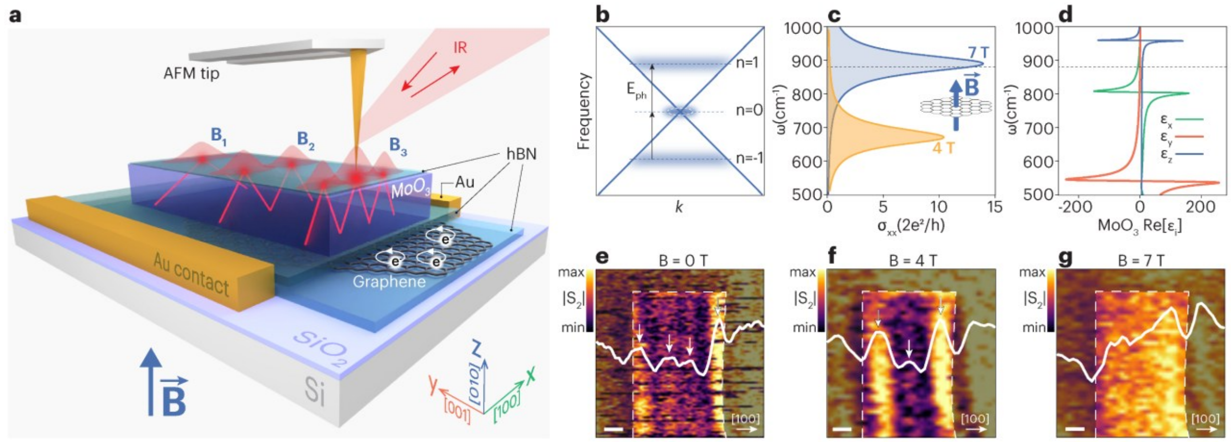

Fig. 1 | Experimental observation of LPPs with m-SNOM. a Scheme of cryogenic m-SNOM of a vdW heterostructure composed of MoO_3 on top of a hBN/graphene/hBN stack. An additional protective hBN layer covers the whole device. IR beam is focused on the apex of a tip whose near fields interact with the sample. A perpendicular magnetic field is applied to the sample, inducing cyclotron motion of charges in graphene and modifying the resulting near-field pattern in the heterostructure. **b** Representation of Landau Levels ($n = -1, 0, 1$) in graphene's Dirac cone. Photons with energy $E_{ph} = |E_{\pm 1} - E_0|$ excite a state from $n = -1$ to $n = 0$ or $n = 0$ to $n = 1$ when graphene is at charge neutral. This should not be confused with a direct two-photon process from $n = -1$ to $n = 1$. **c** Longitudinal optical conductivity of graphene in the presence of a transverse magnetic field. The inset shows a schematic of the transverse magnetic field perpendicular to the graphene plane. **d** Real part of the diagonal components of α-MoO_3's dielectric tensor. (**e-g**) m-SNOM images of the heterostructure measured at 880 cm^{-1} (indicated by dashed lines in **c** and **d**) at B=0 T and 295 K (**e**), at B=4 T and 150 K (**f**), and at B=7 T and 150 K (**g**). The colormap outside the α-MoO_3 crystal was intentionally greyed out for enhanced visual clarity. The full white lines represent integrated line profiles along the x-axis of MoO_3, while the white arrows indicate near-field maxima. The white dashed line marks the edge of the MoO_3 crystal. The white scale bars represent 200 nm.

The strong tunability of the hybridized mode can be simulated in the transfer matrix approach. In Figure 2, we show the magnetic field dependence of the simulated LPP momenta at 880 cm^{-1}. The LPP momenta is expressed as maxima of the imaginary part of the Fresnel reflection coefficient, $Im[r_p]$ (see Methods section for the optical constants of the materials). The result along the x-axis is shown in Figure 2a. At small fields (B $\leq$ 1.8 T), several abrupt changes in LPPs' momenta are observed, indicating the presence of Landau transitions of higher indices (e.g., $i = -1, j = 2$), previously explored in hBN/graphene systems[24]. As the magnetic field increases beyond 2 T, the LPPs become less confined, manifested in the lower momentum dispersion. When E_{ph} is close to the first LL transition (around 6.8 T), a second LPP branch of higher momenta emerges. In this scenario, both modes coexist simultaneously, albeit weakly. The avoided crossing in the LPP dispersion is a signature of strong coupling between HPhP in α-MoO_3 and LL transitions in graphene. A large Rabi splitting of $\Omega = 50 \pm 2$ cm^{-1} was estimated for 6 T, which satisfies the requirement for strong coupling (see Supporting Information). For higher fields (B ≥

7 T), the more confined LPP branch becomes dominant, and their momenta decreases until it reaches a plateau.

The near-field profiles can be predicted by modeling the m-SNOM experiment using the calculated dispersion from Figure 2a. Our model utilizes the Fourier-transform of the $Im[r_p]$ map as a signal for tip-launched waves that propagate and reflect multiple times at the cavity walls (see Supporting Information for details). Here, we used $v_F = 1.15 \times 10^6$ m/s for better agreement with the experiment. This value is consistent with other works that report the Fermi velocity of graphene encapsulated in hBN[37,38]. Figure 2b shows the simulated map of near-field profiles for a 1 µm cavity as a function of the magnetic field. The distance between fringes varies with the magnetic field strength, consistent with the expected dependence on LPP dispersion. Around 6 T, an additional high-momentum mode can be seen at the edges of the cavity, confirming the presence of two separate branches of LPPs. For fields greater than 7 T, an increased number of peaks is predicted. Our model calculation agrees well with line profiles derived from experiments, as shown in Figure 2c (Model) and Figure 2d (Experiment). This good agreement confirms that the near-field profiles in Figure 2d result from Fabry-Perot (FP) cavity resonances of LPPs in a truncated heterostructure.

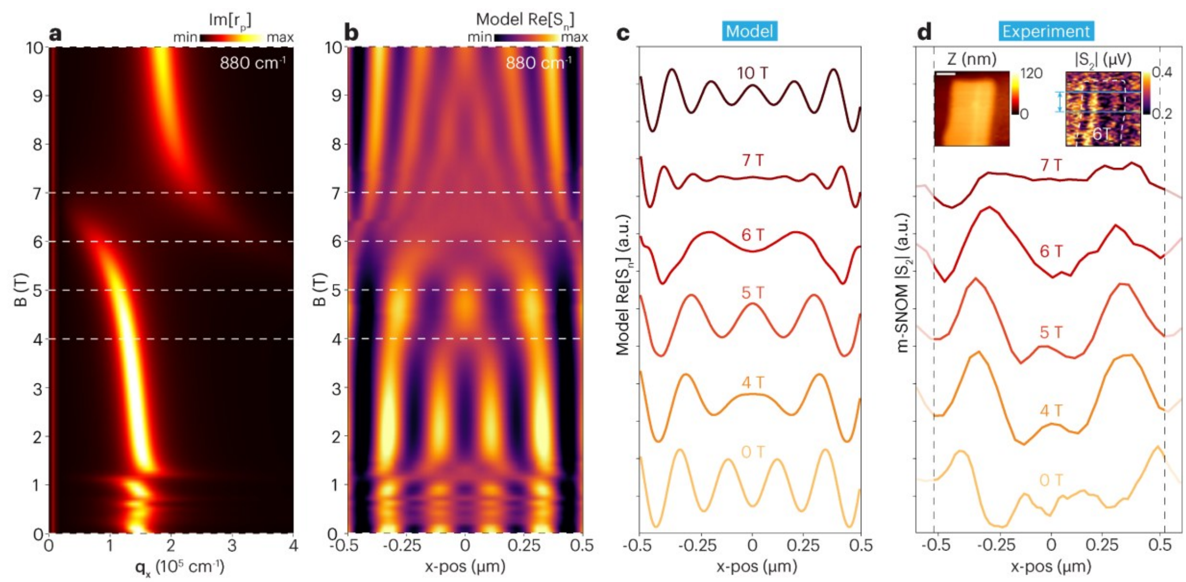

Fig. 2 | Experimental and modeled LPP standing waves in the magnetically tuned nanophotonic cavity. a Calculated polariton momentum at 880 cm^{-1} as a function of the magnetic field. **b** Calculated near-field pattern of polariton modes in a truncated heterostructure of the same dimensions as Figure 1(**e-f**). **c** Modeled $|S_2|$ profiles extracted at the dashed white lines in (**b**). **d** Integrated m-SNOM $|S_2|$ profiles. The grey dashed lines illustrate the edges of the cavity. The inset shows the topography (left) and the $|S_2|$ image (right) of α-MoO_3 at 6 T and 150K. The blue lines in the inset define the region where the signal was integrated.

We proceed to address the spectral content of the cavity. We calculate the frequency dependent LPP dispersion for various magnetic field strengths. The results for 0 T, 5 T, 6 T, and 7 T are displayed in Figure 3a. The fundamental branch of the HPhP is continuously blue shifted with the magnetic field until it reaches 7 T, when it splits into two branches. To present the cavity modes in real space, we employ a Finite-Difference Time-Domain (FDTD) method to simulate spatial-spectral maps of the cavity modes at different magnetic field strengths (Figure 3b). The simulation represents the tip as a point dipole source, which serves as a polariton launcher for the device. By scanning the dipole along the x-direction and recording the near-field electric field underneath it, we simulate the spectral response of the m-SNOM experiment (see Methods for details). The zero-field linescan reproduces the typical behavior of polaritonic cavities, where near-field maxima occur at the resonant frequencies (ω_{res}) of the cavity. The condition for resonance is satisfied when the LPP travels a complete round-trip modulo 2π in phase, i.e. $2qW + 2\phi = 2m\pi$, where m is an integer, W is the cavity width and ϕ is a picked-up phase due to the polariton reflection. As the magnetic field increases, the ω_{res} shift to higher frequencies, and the cavity becomes more lossy.

Figures 3c displays both experimental and simulated line profiles at two different frequencies for 0, 5, 6 T and 7 T. We observe that from 0 T to 6 T, the number of peaks at 880 cm^{-1} gradually drops from 4 to 2, while at 860 cm^{-1}, it drops from 2 to 1. This heightened sensitivity of higher frequency modes to magnetic fields corroborates with the increased λ_p tunability of more confined LPPs, calculated in Figure 3a. This conclusion can also be reached by noticing that the increased density of states of HPhP at higher frequencies leads to a more efficient coupling with the DiME. Moreover, despite the increased mode damping at 7 T, the number of peaks increases again for 860 cm^{-1}, indicating the cavity is dominated by the lower LPP branch, red-shifted from the original HPhP mode.

We estimate the ω_{res} and quality factor (Q) of the cavity by extracting near-field spectra from Figure 3b, with the dipole positioned at the center of the cavity. Figure 3d displays these spectra for four different magnetic field strengths. Due to the mirror symmetry of the source-sample system, only odd values of the FP resonance order (m) appear. The spectral position of the peaks provides the ω_{res} while their widths ($\Delta\omega$) relate to the polariton lifetime. Figure 3e shows the simulated near-field spectra for a range of magnetic fields. As previously mentioned, ω_{res} for higher values of m changes more rapidly with the magnetic field. As the photon energy approaches E_1 (indicated by red line in Figure 3e), the resonances become indistinguishable. To calculate the quality factor of the cavity ($Q = \omega_{res}/\Delta\omega$) we extract the peak and width of the first resonance order ($m = 1$). As shown in Figure 3f, the quality factor decreases as the photon energy approaches the Landau transition and recovers its value after 7 T. Even though the LPPs are more confined at 7 T, the cavity maintains a high Q, comparable to the values observed when no magnetic field is applied.

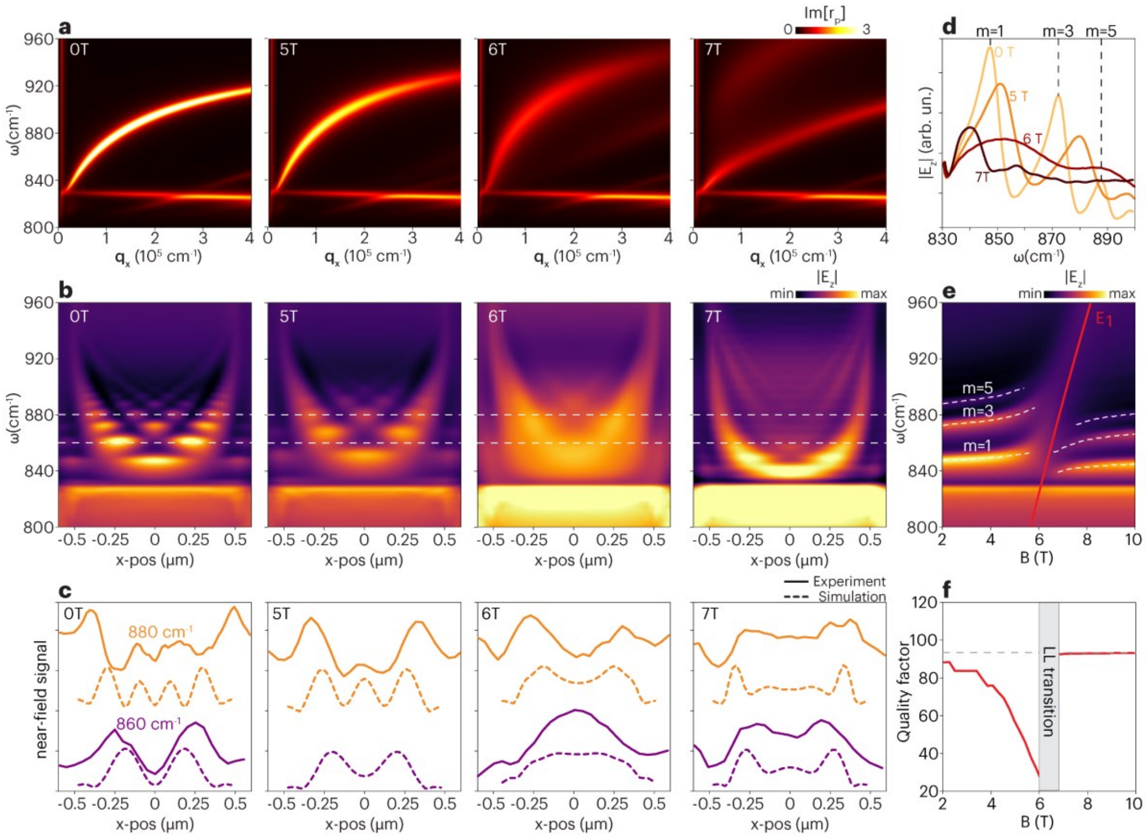

Fig. 3 | LPPs dispersion with the magnetic field and its impact on the cavity modes across the LL transition. a Dispersion of LPPs expressed as Im[r_p] for 0 T, 5 T, 6T and 7 T, for the same heterostructure described in Figure 1(**a**). **b** Simulated spectral-linescans across the 1 µm wide α-MoO_3 ribbon. The dashed white lines indicate the frequencies where line-profiles were extracted. **c** Experimental (solid) and simulated (dashed) line profiles for two different frequencies. **d** Near-field spectra for different magnetic fields obtained from (**b**) at x=0 position. The black dashed lines indicate the position of the resonant frequencies at 0 T for different resonance orders. **e** Simulated near-field spectra for a range of magnetic fields. The simulation was performed with the dipole being at zero position. The white dashed lines indicate the resonant frequencies for different m and the red line represents the energy of the first LL. **f** Calculated quality-factor as a function of magnetic field for m=1. The grey dashed line represents the quality factor of the cavity at zero field.

To further explore the potential of tunable biaxial properties in an ideal cavity, we calculate the LPPs' dispersion along both in-plane directions of α-MoO_3. Here we used the same heterostructure as shown in Figure 1a but with an idealized small square cavity with low-loss graphene (see Methods for details). The dispersions at 0.1 T, 6.4 T and 8 T, are displayed in Figures 4a-c, respectively. At low fields, the cavity is dominated by the HPhP response in α-MoO_3. In this scenario, the polaritons do not propagate in the y-direction, as the in-plane wave-vector only presents a q_x component. However, at 6 T, another mode appears in the y-direction. This branch, originated from DiMEs in graphene, can be tuned with the magnetic field, allowing the propagation of LPPs in both x- and y- directions. Moreover, because the LPPs dispersion in the x-direction can also be adjusted with the magnetic field, we can control their wavefront profiles in real space. As the magnetic field is increased further to 8 T, the DiME resonance is blue shifted, interacting only weakly with the HPhP fundamental branch.

The cavity modes manifest a dramatic change of mode profiles driven by magnetic field, as shown in real-space simulations (Figure 4d, see Methods for details of the simulation). The simulations at 880 cm^{-1} clearly demonstrate a variation of the field distribution of a 2×2 μm^2 α-MoO_3 square cavity with the magnetic field. At 0.1 T, the constructive interference of the anisotropic HPhP in α-MoO_3 leads to a standing pattern along the x-direction. At 6 T the simulation exhibits hot spots of electric field along both in-plane directions, suggesting the change of topology of the LPPs IFC from hyperbolic to elliptical. This is further elucidated at 6.4 T where we observe circular fringes propagating from the origin. For higher magnetic field values (beyond 7 T), the LPP becomes hyperbolic again due to a mismatch of E_{ph} and E_1. The difference in mode confinement for 7 T and 8 T corroborates with the calculated dispersion on Figure 2a.

The magnetically induced topological transition of the cavity nature between hyperbolic and elliptical IFC can also be identified in the momentum space (defined by $\overrightarrow{q_x} \times \overrightarrow{q_y}$). In Figure 4e, we analyze the Fourier transform of the cavity mode profile in Figure 4d and demonstrate an explicit transition from a hyperbolic to an elliptical dispersion, and again to hyperbolic at 7 T and 8 T. The beating pattern at 0.1 T and 8 T for higher momenta suggests the cavity supports resonant modes of higher orders as well. This does not occur at 6 T and 6.4 T since the wavevector of LPPs is limited by its elliptical dispersion. Moreover, despite the elliptical dispersion at 6.0 T, the dispersion is primarily concentrated at a single pair of $\pm q_x$ values. This restriction in momentum space at 6 T can be characterized as a polariton canalization phenomenon and is more clearly illustrated in semi-infinite α-MoO_3 slabs (see Supporting Information for additional simulations). Thus, our results suggest a magnetically tunable spatial distribution of the cavity modes via topology transitions in the LPP IFC.

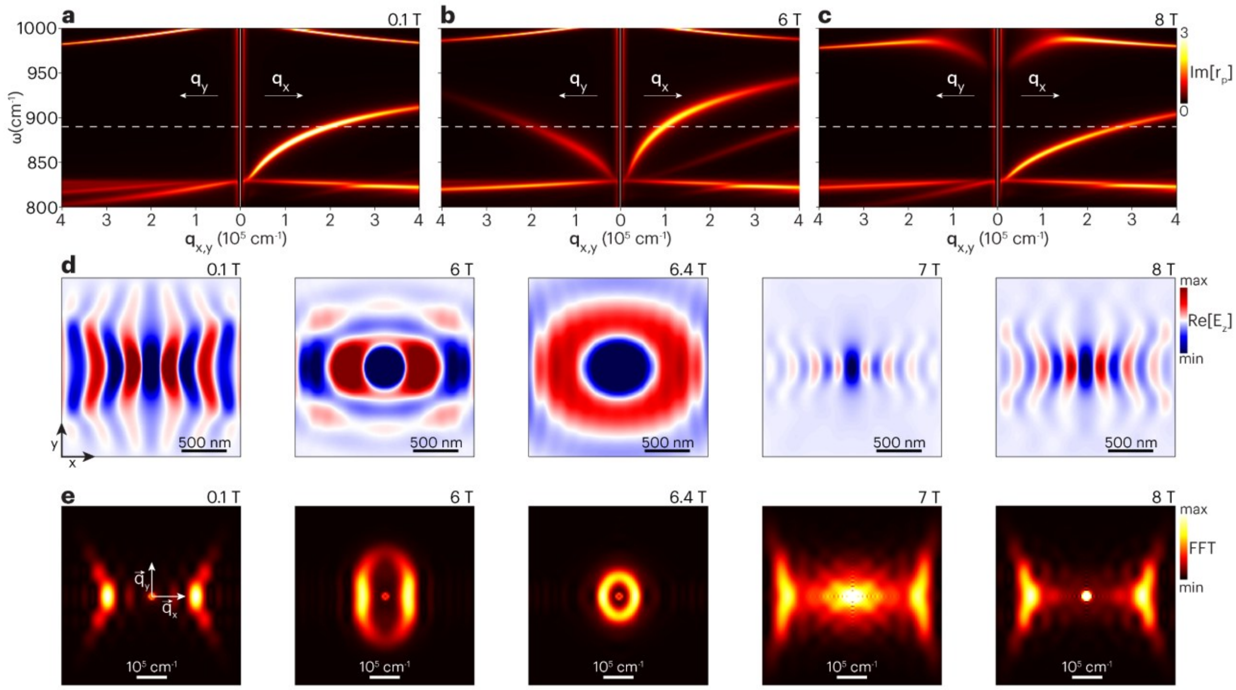

Fig. 4 | Magnetically induced photonic topological transition. Dispersion of LPPs along the y- (q_y to the left side) and x-directions (q_x to the right side) of α-MoO_3. The dispersion is represented as Im[r_p] for **a** 0.1 T, **b** 6 T, and **c** 8 T for the same heterostructure described in Figure 1(**a**). **d** Real-space simulations of LPP near-fields launched by a dipole source at the frequency of 880 cm^{-1} (marked as white dashed lines in a-c) for different magnetic fields. **e** Spatial Fourier transform of **d** in q-space.

In this work, we introduce the magnetic field as a new degree of freedom for controlling polaritonic cavity modes in vdW heterostructures. The LPP-based polariton cavities exhibit excellent wavelength tunability, surpassing the limits in highly doped plasmonic systems that are typically in the weak coupling regime. Furthermore, we explored the magnetic topological transition of the LPPs' IFC as a plausible mechanism to regulate the spatial distribution of cavity modes. We note several alternative material platforms beyond MoO_3/graphene that could also support tunable, anisotropic polaritonic cavities. These include multilayer structures (hBN-MoO_3-G-MoO_3-G-MoO_3-hBN), β-Ga_2O_3, V_2O_5, and G–CrSBr heterostructures, each of which offers unique dielectric anisotropies and excitonic or phononic resonances that may be engineered for future realizations of magnetically tunable polariton cavity topologies[39–41]. Thus, our study highlights the versatility of spatially restricted LPP resonances for an enhanced control of light-matter interactions at the nanoscale. The development of cryogenic m-SNOM opens opportunities for exploring new cavity control mechanisms, such as those based on Cooper pair polaritons and magnon polaritons. By combining magnetic polaritons in cavities with low-symmetry environments[42,43] or Moiré systems[44], intriguing phenomena such as non-reciprocal cavities may emerge, enabling novel control in the spatial distribution of the cavity modes.

Supporting Information: (1) Sample fabrication, (2) Magneto-SNOM (m-SNOM), (3) Numerical Methods, (4) Strong coupling of phonon polaritons with Landau transitions, (5) Numerical model of the near-field signal in polaritonic cavities, (6) Comparison with SPP-HPhP cavity, (7) Real-space simulations of LPPs in semi-infinite biaxial media, (8) Electrical characterization of heterostructure, and (9) Optical microscope image of the device.

Research on developing the programable polariton cavities is primarily supported as part of Programmable Quantum Materials (Pro-QM), an Energy Frontier Research Center (EFRC) funded by the U.S. Department of Energy (DOE), Office of Science, Basic Energy Sciences (BES), under award DE-SC0019443. R.A.M. and R.O.F thank support by São Paulo Research Foundation (FAPESP) through grants 2020/15740-3 and 2022/06709-0, and Young Investigator grant 2019/14017-9. M.K.L. acknowledges Gordon and Betty Moore Foundation DOI: 10.37807/gbmf12258 for supporting the development of m-SNOM scanning probe systems and polaritonic materials, and the support for near-field platforms for probing electrodynamics in chiral materials from the NSF Faculty Early Career Development Program under Grant No. DMR – 2045425. D.N.B, M.K.L., L.W. acknowledge funding by the U.S. Department of Energy, Office of Science, National Quantum Information Science Research Centers, Co-design Center for Quantum Advantage (C2QA) under contract number DE-SC0012704 for support of the data analysis. J.A.F. acknowledges the National Science Foundation under Award Number 2103721. R.O.F acknowledges CNPq (grant 309946/2021-2) for supporting the interaction. R.A.M., A.R.C. and R.O.F. acknowledge the Brazilian Synchrotron Light Laboratory and the Brazilian Nanotechnology National Laboratory, both part of the Brazilian Centre for Research in Energy and Materials (CNPEM), a private non-profit organization under the supervision of the Brazilian Ministry for Science, Technology, and Innovations (MCTI) - (MNF/Proposals: 20221652, 20230074, and LAM/Proposal: 20221645), as well as Ingrid D. Barcelos and Marcelo R. Piton for the support with initial sample fabrication. X.D acknowledges the National Science Foundation under Award Number 2104781.

At the time of publication, X.C. is associated with Flexcompute Inc., the company behind the Tidy3D simulation software utilized in this research. This connection has not affected the study's design, data

collection and analysis, publication decisions, or manuscript preparation. The remaining authors have no competing interests to disclose.

1. Brune, M. *et al.* Quantum Rabi Oscillation: A Direct Test of Field Quantization in a Cavity. *Phys Rev Lett* **76**, 1800–1803 (1996).
2. Basov, D. N., Fogler, M. M. & García de Abajo, F. J. Polaritons in van der Waals materials. *Science* **354**, aag1992 (2016).
3. Sternbach, A. J. *et al.* Negative refraction in hyperbolic hetero-bicrystals. *Science* **379**, 555–557 (2023).
4. Hu, H. *et al.* Gate-tunable negative refraction of mid-infrared polaritons. *Science* **379**, 558–561 (2023).
5. Zhang, T., Zheng, C., Chen, Z. N. & Qiu, C.-W. Negative Reflection and Negative Refraction in Biaxial van der Waals Materials. *Nano Lett* **22**, 5607–5614 (2022).
6. Li, P. *et al.* Collective near-field coupling and nonlocal phenomena in infrared-phononic metasurfaces for nano-light canalization. *Nat Commun* **11**, 3663 (2020).
7. Duan, J. *et al.* Multiple and spectrally robust photonic magic angles in reconfigurable α-MoO3 trilayers. *Nat Mater* **22**, 867–872 (2023).
8. Obst, M. *et al.* Terahertz Twistoptics–Engineering Canalized Phonon Polaritons. *ACS Nano* **17**, 19313–19322 (2023).
9. Li, P. *et al.* Hyperbolic phonon-polaritons in boron nitride for near-field optical imaging and focusing. *Nat Commun* **6**, 7507 (2015).
10. Chikkaraddy, R. *et al.* Single-molecule strong coupling at room temperature in plasmonic nanocavities. *Nature* **535**, 127–130 (2016).
11. Herzig Sheinfux, H. *et al.* High-quality nanocavities through multimodal confinement of hyperbolic polaritons in hexagonal boron nitride. *Nat Mater* **23**, 499–505 (2024).
12. Autore, M. *et al.* Boron nitride nanoresonators for phonon-enhanced molecular vibrational spectroscopy at the strong coupling limit. *Light Sci Appl* **7**, 17172 (2018).
13. Emmanuele, R. P. A. *et al.* Highly nonlinear trion-polaritons in a monolayer semiconductor. *Nat Commun* **11**, 3589 (2020).
14. Gu, J. *et al.* Enhanced nonlinear interaction of polaritons via excitonic Rydberg states in monolayer WSe2. *Nat Commun* **12**, 2269 (2021).
15. Hennessy, K. *et al.* Quantum nature of a strongly coupled single quantum dot–cavity system. *Nature* **445**, 896–899 (2007).
16. Yu, S.-J. *et al.* Ultrahigh-Quality Infrared Polaritonic Resonators Based on Bottom-Up-Synthesized van der Waals Nanoribbons. *ACS Nano* **16**, 3027–3035 (2022).
17. Barcelos, I. D. *et al.* Ultrabroadband Nanocavity of Hyperbolic Phonon–Polaritons in 1D-Like α-MoO_3. *ACS Photonics* **8**, 3017–3026 (2021).

18. Zeng, Y. *et al.* Tailoring Topological Transitions of Anisotropic Polaritons by Interface Engineering in Biaxial Crystals. *Nano Lett* **22**, 4260–4268 (2022).

19. Ruta, F. L. *et al.* Surface plasmons induce topological transition in graphene/α-MoO3 heterostructures. *Nat Commun* **13**, 3719 (2022).

20. Jia, Y. *et al.* Tunable Plasmon–Phonon Polaritons in Layered Graphene–Hexagonal Boron Nitride Heterostructures. *ACS Photonics* **2**, 907–912 (2015).

21. Woessner, A. *et al.* Highly confined low-loss plasmons in graphene–boron nitride heterostructures. *Nat Mater* **14**, 421–425 (2015).

22. Dai, S. *et al.* Graphene on hexagonal boron nitride as a tunable hyperbolic metamaterial. *Nat Nanotechnol* **10**, 682–686 (2015).

23. Barcelos, I. D. *et al.* Infrared Fingerprints of Natural 2D Talc and Plasmon-Phonon Coupling in Graphene-Talc Heterostructures. *ACS Photonics* **5**, 1912–1918 (2018).

24. Wehmeier, L. *et al.* Landau-phonon polaritons in Dirac heterostructures. *Sci Adv* **10**, 3487 (2024).

25. Keilmann, F. & Hillenbrand, R. Near-field microscopy by elastic light scattering from a tip. *Philos Trans A Math Phys Eng Sci* **362**, 787–805 (2004).

26. Luo, C. *et al.* Probing Polaritons in 2D Materials. *Adv Opt Mater* **8**, 1901416 (2020).

27. Barcelos, I. D. *et al.* Probing Polaritons in 2D Materials with Synchrotron Infrared Nanospectroscopy. *Adv Opt Mater* **8**, 1–16 (2020).

28. Hu, D., Luo, C., Kang, L., Liu, M. & Dai, Q. Few-layer hexagonal boron nitride as a shield of brittle materials for cryogenic s-SNOM exploration of phonon polaritons. *Appl Phys Lett* **120**, 161101 (2022).

29. Zhang, Y. *et al.* Landau-level splitting in graphene in high magnetic fields. *Phys Rev Lett* **96**, 136806 (2006).

30. Song, Y. J. *et al.* High-resolution tunnelling spectroscopy of a graphene quartet. *Nature* **467**, 185–189 (2010).

31. Dapolito, M. *et al.* Infrared nano-imaging of Dirac magnetoexcitons in graphene. *Nat Nanotechnol* **18**, 1409–1415 (2023).

32. Jiang, Z. *et al.* Infrared Spectroscopy of Landau Levels of Graphene. *Phys Rev Lett* **98**, 197403 (2007).

33. Zheng, Z. *et al.* A mid-infrared biaxial hyperbolic van der Waals crystal. *Sci Adv* **5**, 1–9 (2019).

34. Chen, M. *et al.* Configurable phonon polaritons in twisted α-MoO3. *Nat Mater* **19**, 1307–1311 (2020).

35. Hu, G. *et al.* Topological polaritons and photonic magic angles in twisted α-MoO3 bilayers. *Nature* **582**, 209–213 (2020).

36. Hu, H. *et al.* Doping-driven topological polaritons in graphene/α-MoO3 heterostructures. *Nat Nanotechnol* **17**, 940–946 (2022).

37. Faugeras, C. *et al.* Landau level spectroscopy of electron-electron interactions in graphene. *Phys Rev Lett* **114**, 126804 (2015).

38. Nedoliuk, I. O., Hu, S., Geim, A. K. & Kuzmenko, A. B. Colossal infrared and terahertz magneto-optical activity in a two-dimensional Dirac material. *Nat Nanotechnol* **14**, 756–761 (2019).

39. Matson, J. *et al.* Controlling the propagation asymmetry of hyperbolic shear polaritons in beta-gallium oxide. *Nat Commun* **14**, 5240 (2023).

40. Taboada-Gutiérrez, J. *et al.* Broad spectral tuning of ultra-low-loss polaritons in a van der Waals crystal by intercalation. *Nat Mater* **19**, 964–968 (2020).

41. Ruta, F. L. *et al.* Hyperbolic exciton polaritons in a van der Waals magnet. *Nat Commun* **14**, 8261 (2023).

42. Passler, N. C. *et al.* Hyperbolic shear polaritons in low-symmetry crystals. *Nature* **602**, 595–600 (2022).

43. Galiffi, E. *et al.* Extreme light confinement and control in low-symmetry phonon-polaritonic crystals. *Nat Rev Mater* **9**, 9–28 (2023).

44. Moore, S. L. *et al.* Nanoscale lattice dynamics in hexagonal boron nitride moiré superlattices. *Nat Commun* **12**, 5741 (2021).